Batteries & Supercaps

Research Article
doi.org/10.1002/batt.202300032

Chemistry Europe
European Chemical
Societies Publishing

www.batteries-supercaps.org

Fracture Testing of Lithium-Ion Battery Cathode Secondary Particles in-situ inside the Scanning Electron Microscope

Laura Wheatcroft,*[a, d] Arron Bird,[a] Joe C. Stallard,[b, d] Ria L. Mitchell,[a] Samuel G. Booth,[a, d, e] Alisyn J. Nedoma,[c, d] Michael F. L. De Volder,[b, d] Serena A. Cussen,[a, d] Norman A. Fleck,[b, d] and Beverley J. Inkson*[a, d]

Fracture of cathode secondary particles is a critical degradation mechanism in lithium-ion batteries. The microindentation strength of $LiNi_{0.8}Mn_{0.1}Co_{0.1}O_2$ secondary particles is measured in situ in the scanning electron microscope (SEM), enabling dynamical imaging of fracture. Crack propagation is intergranular between primary particles when induced by compressing between flat platens (analogous to calendaring), and with a cono-spherical indenter (representing particle-particle contact). Fracture occurs directly beneath the cono-spherical tip and at the centre of secondary particles when compressed between flat platens. Finite element modelling of stress states provides insight into the dependence of fracture load upon cohesive strength and particle toughness. Secondary particle indentation strength decreases with increasing secondary particle size, with cycling, and with increasing state of charge. The indentation strength decrease is greatest in earlier stages of delithiation. The novel microindentation technique allows assessment of strength and toughness of different cathode morphologies, aiding prediction of optimal particle structure and processing conditions.

Introduction

$LiNi_xMn_yCo_zO_2$ (NMC) materials are considered key candidates of choice as cathode active materials for electric vehicles, owing to their high theoretical capacity (270 mAh g^{-1}).[1,2] Higher nickel contents not only reduce reliance on expensive elements such as cobalt, which represent supply chain risks, but also offer higher capacities.[3] However, Ni-rich NMC materials also face

[a] Dr. L. Wheatcroft, A. Bird, Dr. R. L. Mitchell, Dr. S. G. Booth,
    Prof. S. A. Cussen, Prof. B. J. Inkson
    Department of Materials Science and Engineering
    University of Sheffield
    Mappin Street, Sheffield, S1 3JD (United Kingdom)
    E-mail: l.j.wheatcroft@sheffield.ac.uk
            beverley.inkson@sheffield.ac.uk
[b] Dr. J. C. Stallard, Prof. M. F. L. De Volder, Prof. N. A. Fleck
    Department of Engineering
    University of Cambridge
    Trumpington Street, Cambridge, CB2 1PZ (United Kingdom)
[c] Dr. A. J. Nedoma
    Department of Chemical and Biological Engineering
    University of Sheffield
    Mappin Street, Sheffield, S1 3JD (United Kingdom)
[d] Dr. L. Wheatcroft, Dr. J. C. Stallard, Dr. S. G. Booth, Dr. A. J. Nedoma,
    Prof. M. F. L. De Volder, Prof. S. A. Cussen, Prof. N. A. Fleck, Prof. B. J. Inkson
    Faraday Insititution
    Quad One,
    Harwell Campus, Didcot, OX11 0RA (United Kingdom)
[e] Dr. S. G. Booth
    Integrated Graphene Ltd
    Euro House,
    Stirling, FK8 2DJ (United Kingdom)

considerable challenges in terms of prolonging both lifetime and performance. Such Ni-rich chemistries are, for example, prone to increased fracture during cycling which can impinge on the ability to predict long term performance.[3] A deeper understanding of the fracture mechanics occurring in Ni-rich cathodes is needed to determine how these effects manifest and also provide a set of guiding principles for the synthesis of more robust cathode materials.

Fracture mechanisms within cathode materials are complex. Previous publications report that cracks can be induced by phase changes within single particles initiated by strain mismatch between the unit cells of different phases,[4] or via surface phase transformations from layered to rock salt structures resulting from electrolyte reactions with the cathode active particle,[5] and/or oxygen release at high states of charge,[6] or from the pile-up of dislocations within particles.[8] Cracks are also known to form as early as the first charge cycle.[8] Particle fracture is detrimental to battery performance as cracks cause fresh cathode active surface to be exposed to the electrolyte and thereby degrade.[9] Portions of the cathode particle can become electrically disconnected from the bulk.[9,10] In both cases, the net result is capacity loss.[9,10]

NMC materials that have been manufactured by the co-precipitation method typically form a 'meatball-type' structure of densely packed primary particles assembled into a secondary particle 'meatball'. Cracking between the primary particles is termed intergranular cracking and is often observed as a fracture mechanism in NMC materials.[11–13] Intergranular cracking in NMCs is observed to a greater extent with increasing Ni-content,[14] attributed to a large c-axis contraction at high states of charge.[15,16] Dislocation glide within the primary particles can occur during calendaring and initiate intergranular cracking.[17] After cracks have formed, NMC811 particles can become more

Batteries & Supercaps

Research Article
doi.org/10.1002/batt.202300032

Chemistry Europe
European Chemical
Societies Publishing

susceptible to further fracture and subsequent degradation.[14,17,18] The formation of intergranular fractures at high states of charge imposes a practical limit on the cycling window for Ni-rich NMC particles, limiting their energy density.[19] Consequently, there is great interest in understanding fracture mechanisms and finding ways to mitigate fracture to utilise a greater amount of the potential energy density of these materials.

Fracture strength and fracture toughness measurements of individual cathode active particles can be used to correlate the microstructure with its resistance to fracture.[18,20] In previous studies, secondary particles (NMC111) have been loaded with a flat punch to assay their fracture strength,[21] and modulus and fracture toughness have been measured with nanoindentation experiments on NMC532 and NMC811.[14,22]

Traditional nanoindentation experiments do not provide the opportunity to image the fracture mechanism during loading; consequently, interpretation of the sequence of failure events is a challenge. Here, we present a novel method for assessing the resistance to fracture of individual cathode particles by performing in situ SEM microindentation. Use of SEM imaging enables the advance of fracture mechanisms to be imaged in-real time. Indentation was performed with both cono-spherical and flat platen indentation tips, with the choice of tip altering the stress state and consequently the fracture mechanism which can be studied. Flat platen indentation is analogous to calendaring between large diameter rolls, where-

as the cono-spherical tip approximates the contact conditions between neighbouring particles.[23] Particle microindentation enables the strength to be measured, and in situ SEM imaging enables the dynamical fracture mechanism to be observed during fracture. By interpreting the experimental results with a mechanical model, we provide estimates of the secondary particle toughness and fracture strength. Indentation tests were also performed on NMC811 cathode particles extracted from electrodes at different states of charge to correlate particle strength with lithium occupancy.

Results and Discussion

In situ mechanical testing of individual cathode particles

Dynamic indentation testing was carried out on individual $LiNi_{0.8}Mn_{0.1}Co_{0.1}O_2$ (NMC811) particles supported by a Si substrate whilst continuous SEM images of the mechanical failure mechanisms were obtained. Example snapshots of the dynamical SEM indentation of a typical pristine NMC811 cathode secondary particle are shown in Figure 1(a–c). For such tests, the indentation load was applied using a cono-spherical indentation tip; the magnitude of uniaxial load P during testing is labelled in Figure 1(a–c), with the resultant measured load-displacement response from the test given in Figure 1(d). The load and displacement both increase until intergranular

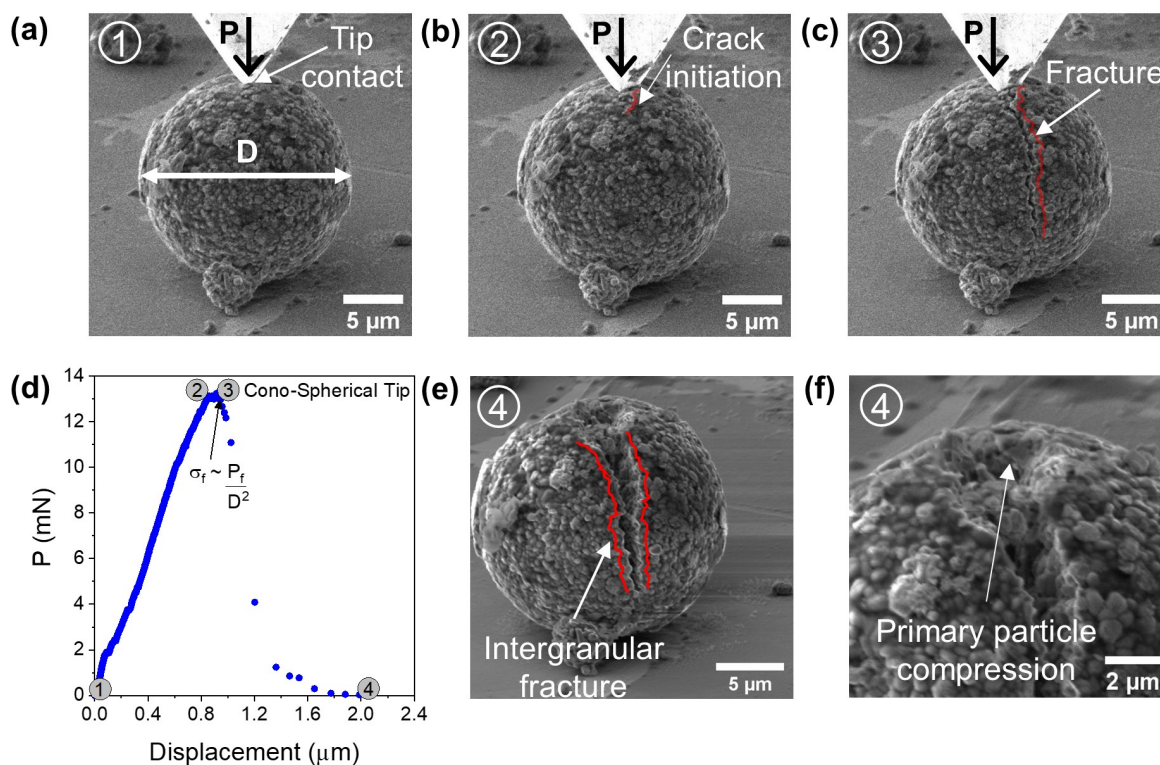## Fracture of a Pristine NMC811 Particle *in-situ* SEM

Figure 1. a–c) SEM images of a pristine NMC811 particle taken at different points during indentation (1, 2, and 3, respectively) on the load-displacement curve in (d). e) Image of the particle post-fracture at point 4 on the load displacement curve, and f) a magnified image of the indentation crater in (e).

Batteries & Supercaps

Research Article
doi.org/10.1002/batt.202300032

Chemistry Europe
European Chemical
Societies Publishing

fracture is visible at the particle surface close to the indentation tip, Figure 1(b). Subsequently, the measured load decreases as intergranular cracking proceeds outwards from the tip-particle contact zone (Figure 1c). Two images of the particle post-indentation are given in Figure 1(e and f). Permanent indentation of the sample surface is evident (Figure 1f), revealing both plastic deformation of the primary NMC grains and a limited degree of intragranular cracking. This result indicates that plasticity around the indentation accompanies fracture.

In-situ SEM indentation testing with flat platen compression was also performed on pristine NMC811 particles (Figure 2). Images of a particle before and after fracture from flat-platen compression are given in Figure 2(a) and (d), respectively. The appearance of the fracture coincides with a sharp drop in the measured load from the peak value. The images of the fracture surface in Figure 2(c and d) suggest that fracture is initiated from the centre of the particle. This contrasts with fracture initiated using the cono-spherical tip, where fracture proceeds from the near surface (Figure 2b). Propagation of fracture in flat platen tests proceeded too quickly to fully resolve the crack opening. Fracture occurred mid-raster on the image slice in Figure 2(c). In contrast to fracture with the flat platen, fracture propagation during cono-spherical indentation was sufficiently slow to be imaged as shown Figure 1(b and c).

The peak load P_f at which intergranular cracking was observed in compressed pristine NMC811 particles is compared for flat platen and cono-spherical indentation as a function of particle diameter in Figure 2(f). The two experiments give distinct trends of increasing peak load with increasing particle diameter. For a similar NMC811 particle diameter, the magnitude of peak load at the onset of intergranular fracture from cono-spherical indentation experiments is significantly below that measured for a flat platen, over the range of particle diameters investigated here (Figure 2f).

The reason for the difference between the cono-spherical and flat platen indentation responses was first explored by prediction of the stress state induced by a cono-spherical indentation tip and under compression with a flat platen, using the commercial finite element software ABAQUS (Dassault Systèmes). For both indenter geometries, axisymmetric elastic simulations were performed on a particle of diameter 10 μm, and of Young's modulus of 200 GPa and Poisson ratio of 0.3; these values are typical of those reported in the literature.[20,22] The silicon substrate was assigned a Young's modulus of 150 GPa and Poisson ratio 0.3.[24] The cono-spherical diamond indenter possessed a tip radius of 0.71 μm, a Young's modulus of 1141 GPa and a Poisson ratio of 0.07.[25]

Contour plots of the hoop stress distribution $\sigma_{\theta\theta}$ predicted by the elastic calculations of cono-spherical indentation and compression with a flat platen are shown in Figure 3(a) and (b), respectively, for an indentation load of 10 mN. The tensile
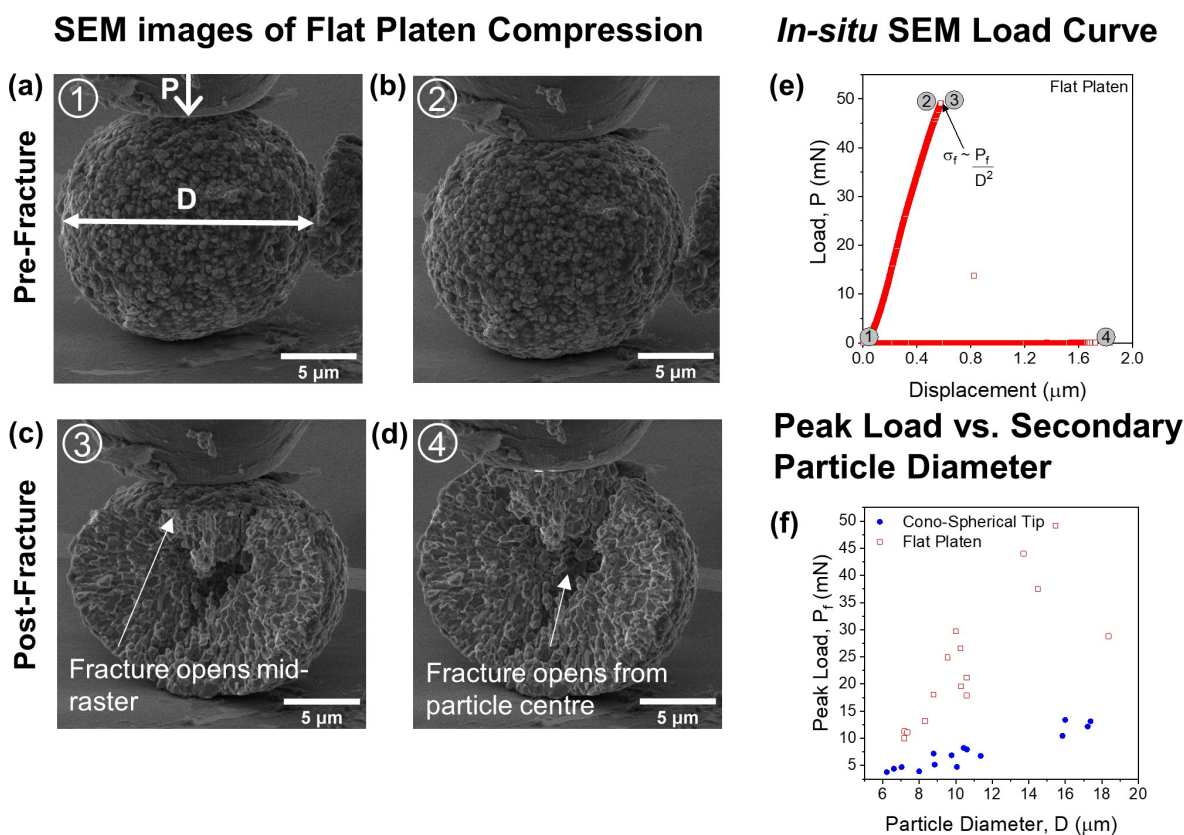
SEM images of Flat Platen Compression

In-situ SEM Load Curve

Peak Load vs. Secondary Particle Diameter

Figure 2. a–d) Dynamical SEM images of particles indented with a flat platen with each image corresponding to the points labelled 1, 2, 3, and 4 on the Load (*P*)-Displacement curve in (e). f) Graph showing Peak Load (*P*$_f$) against secondary particle diameter (*D*) measured by micro-indentation using a flat platen (hollow red squares), and a cono-spherical tip (blue circles).
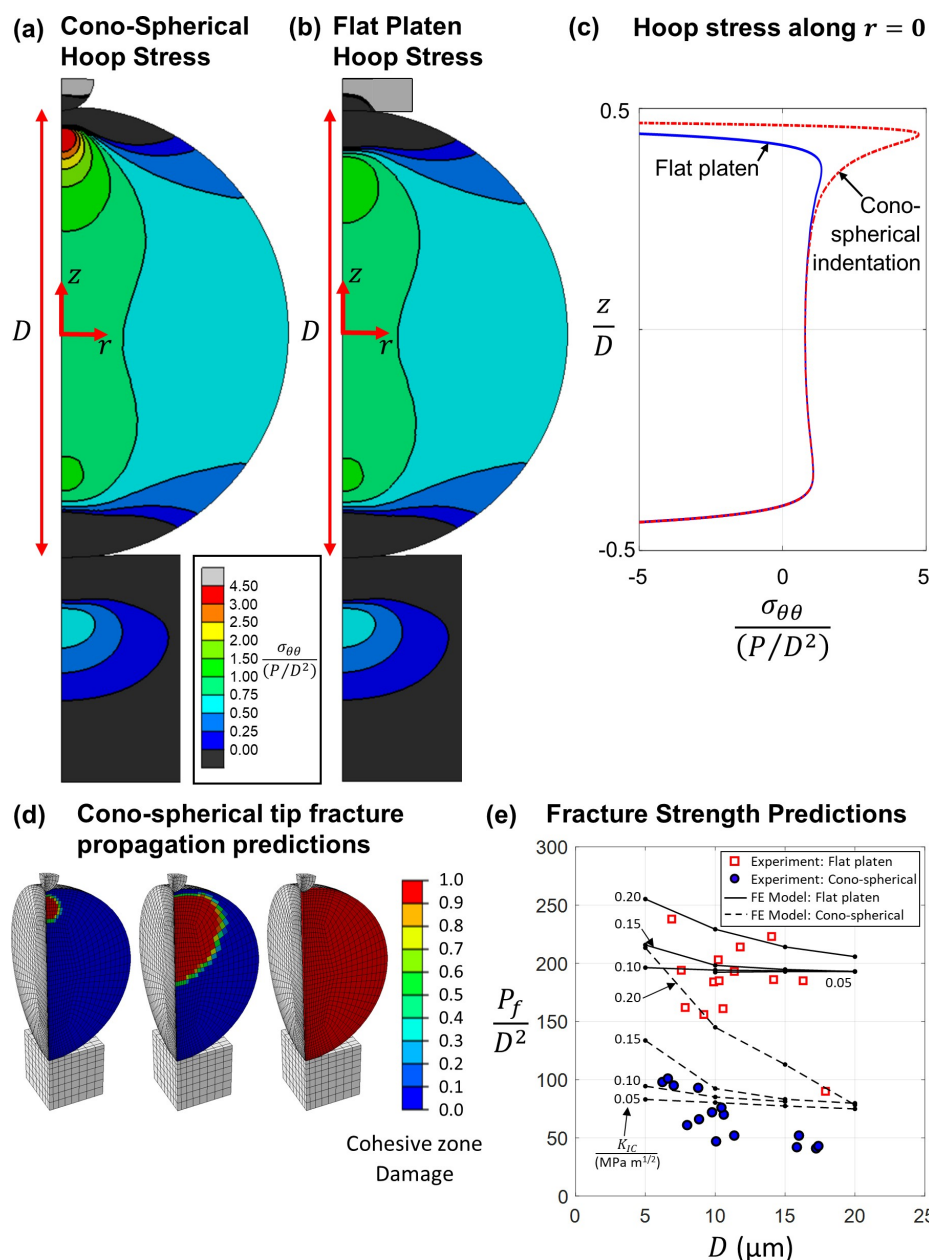
Figure 3. Dimensionless contour plots of hoop (tensile) stress distribution ($\sigma_{\theta\theta}$) predicted by elastic axisymmetric simulation of a 10 μm diameter elastic secondary particle subjected to a) cono-spherical indentation and b) flat platen indentation at load $P = 10$ mN. c) Plot of $\sigma_{\theta\theta}$ along the secondary particle centreline from flat platen and cono-spherical indentation. d) Predictions of the initiation and propagation of fracture upon cono-spherical indentation, and e) comparison of the measured (hollow red square- flat platen, and blue circle- cono-spherical tip) and predicted P_f/D^2 values (solid black and dotted black lines) for NMC811 secondary particle fracture.

stress $\sigma_{\theta\theta}$ along the line of loading scales with diameter D and the load P as Equation (1).[26]

$$\sigma_{\theta\theta} \approx \frac{P}{D^2} \qquad (1)$$

The tensile stress $\sigma_{\theta\theta}$ predicted along the line of load under the indenter is plotted in Figure 3(c) for both indenter geometries, normalised by P/D^2. Immediately below the contact point the stress is compressive, whereas tension is present further towards the particle centre. Flat platen compression

generates an almost uniform tensile stress across much of the diameter (Figure 3b). The relatively uniform tensile stress across the centre of a brittle particle subjected to diametrical compression, such as that predicted here, may cause a central burst of crack propagation from the fast fracture of a pre-existing flaw, consistent with the post-fracture image in Figure 2(c). Consequently, the indentation strength $\sigma_F = P_f/D^2$ is comparable to the tensile burst strength. In a previous study the average indentation strength for individual NMC111 measured by compression of individual NMC111 secondary particles between flat platens was 188 MPa.[21] Here, the

Batteries & Supercaps

Research Article
doi.org/10.1002/batt.202300032

Chemistry
Europe
European Chemical
Societies Publishing

measured mean indentation strength for pristine NMC811 secondary particles under flat platen compression is 207 ± 49 MPa (Figure 3).

A three-dimensional (3D) finite element model of a secondary cathode particle has been constructed in order to predict the progression of cracking under cono-spherical indentation and flat platen indentation. Anticipating that fracture occurs across a diametrical plane (Figure 1c), symmetry allows for a quarter of the secondary NMC811 particle to be modelled, although it is noted that the secondary particles are not always perfectly spherical. A tensile cohesive zone surface is placed on the expected fracture plane. It takes as input a cohesive strength σ_0 and a fracture toughness K_{IC}, and assumes a traction versus displacement jump across a surface of increasing damage. Figure 1 confirms that crack propagation is intergranular in nature; consequently, the primary particle size (grain size) has an influence on the observed fracture toughness by the usual pull-out mechanisms of grains behind an advancing crack tip. Further details of the finite element model are given in the Supporting Information.

Contour plots of the progression of fracture along a diametrical crack plane are presented in Figure 3(d). Activation of the cohesive zone occurs beneath the cono-spherical indentation zone, from where the greatest tensile stress along the line of loading is predicted by the elastic contour plot of Figure 3(a). Subsequent growth of this fracture ensues downwards, giving final diametral cleavage. Predictions of peak strength P_f/D^2 from the finite element simulation are plotted in Figure 3(e), based upon a cohesive strength $\sigma_0 = 200$ MPa and values of fracture toughness in the range $K_{IC} = 0.05$ MPa m$^{1/2}$ to $K_{IC} = 0.2$ MPa m$^{1/2}$ which are consistent with the wider literature.[20] The predicted strength P_f/D^2 decreases with increasing diameter for cono-spherical indentation simulations, which matches the trend observed experimentally for cono-spherical indentation. Mode I failure initiated by a tensile stress at the surface of particles has been modelled and observed resulting from cycling of NMC secondary particles previously.[23,27]

The measured strength P_f/D^2 for diametral compression by flat platens is almost insensitive to the diameter of secondary particle to within scatter, recall Figure 3(e). Finite element simulations support this observation. The predicted strength P_f/D^2 is close to the cohesive strength, and for lower assumed values of fracture toughness the strength is almost insensitive to secondary particle diameter within the range of the experiment (Figure 3e).

Electrochemical cycling

Secondary particles extracted from the electrodes of cells and charged to different potentials were tested to quantify their mechanical strength as a function of their state of charge. Electrodes were used in the uncalendared state to minimise the effect of mechanical damage from electrode processing on mechanical testing results.

Figure 4 shows representative galvanostatic cycling curves for the first three complete cycles (two C/20 formation cycles, and one C/10 cycle to confirm the capacity of the cathode under standard testing conditions). Electrode charging was stopped during the 4th charge (tested charge in Figure 4) and secondary particles harvested from washed electrodes from disassembled coin cells in an Ar filled glove box for mechanical testing at the potentials indicated by 1, 2, 3, and 4 in Figure 4.

The average first cycle gravimetric capacity for all electrodes measured in this study was 201 ± 2 mAh g^{-1}, consistent with other reported gravimetric capacity values in literature.[28] The voltage profiles in Figure 4 are typical of NMC811 Li half-cell voltage profiles.[5,15] The first cycle shows a large overpotential to 3.9 V vs. Li/ Li$^+$, likely due to air exposure during electrode manufacture causing the formation of surface LiCO$_3$ which can impede ionic and electronic transport.[29]

The stopping potentials indicated by 1, 2, 3, and 4 in Figure 4 were selected to measure the effect of the two c-axis expansion/ contraction regimes during NMC811 de-lithiation upon the secondary particle strength. During charging cycles up to potentials < 4.2 V vs. Li/ Li$^+$, the layered Li$_x$MO$_2$-type rhombohedral R$\bar{3}$m NMC811 lattice undergoes a small c-axis expansion, and an a-axis contraction, resulting in minimal unit cell volume changes.[5,15] At potentials > 4.2 V vs. Li/ Li$^+$ c-axis contraction occurs,[5,15] accompanied by smaller a, and b axis contraction. The grey and red areas in Figure 4 represent c-axis contraction and expansion regimes respectively.

Effect of state of charge on NMC811 secondary particle strength

The indentation strength of individual NMC811 secondary particles with different electrochemical histories was determined by first extracting representative particles from electrodes and then compressing to fracture by SEM microindentation using the cono-spherical tip.

The indentation strength of NMC secondary particles P_f/D^2 before and after 3 cycles, and at different states of charge, is
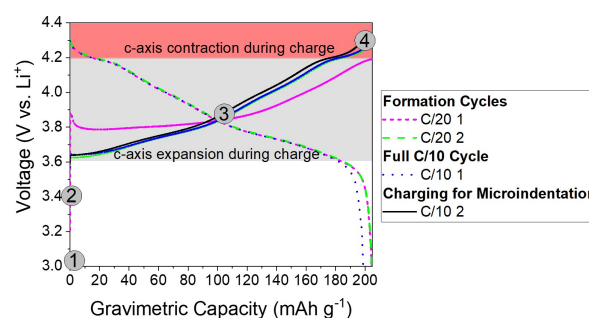

Figure 4. Galvanostatic charge/ discharge curves of NMC811 electrodes cycled between 3.0 V and 4.3 V vs. Li/ Li$^+$. The protocol consisted of two initial formation cycles at C/20 (pink dashes- cycle one, green dots- cycle 2), followed by a complete cycle at C/10 between 3.0 V and 4.3 V vs. Li/ Li$^+$ (blue dots), and a charge at C/10 to 4.3 V. Mechanical testing on cycled cathode secondary particles was performed on the second C/10 charging cycle at the potentials indicated by 1, 2, 3, and 4.

Batteries & Supercaps

Research Article
doi.org/10.1002/batt.202300032

Chemistry Europe
European Chemical
Societies Publishing

presented in Figure 5, with the hardness measured at the point of fracture given in the Supporting Information. 'Pristine' (P) secondary particles are NMC811 secondary particles tested directly from the powder form as received from the manufacturer. All other secondary particles were extracted from PVDF/C65/NMC811 composite electrodes. To evaluate the effects of electrode manufacture, particle removal and electrolyte immersion upon the secondary particle strength, 'Electrode' (E) secondary particles were extracted from an electrode which had not been made into a cell (no electrolyte contact), and 'Electrolyte soaked' (Ex) secondary particles were extracted from an electrode rested at open circuit for 12 h in a half-cell with the electrode infiltrated by electrolyte. The cycled secondary particles were extracted from electrodes charged to different potentials (as indicated in Figure 4). The secondary particle strengths were determined across a range of secondary particle sizes (6–17 μm) from 16 secondary particles for each
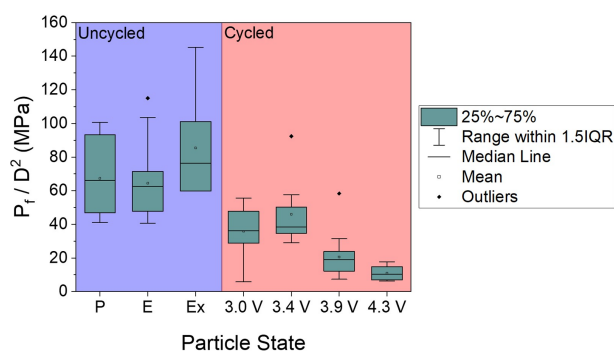

Figure 5. Influence of electrode cycling history on the average indentation strength $\sigma_f = P_f/D^2$ of NMC811 secondary particles. The average strength in the blue region represents secondary particle strength measured from uncycled secondary particles: direct from the manufacturerer (Pristine- P), extracted from an uncycled electrode with no electrolyte contact (Electrode - E), and extracted from an electrode soaked in electrolyte for 12 h (Electrolyte Exposed- Ex). The average strength in the red regions represents secondary particle strength calculated for cycled secondary particles: secondary particles charged to different potentials (3.0 V, 3.4 V, 3.9 V, and 4.3 V vs. Li/Li$^+$) following conditioning cycles. All results presented in Figure 5 were obtained with a cono-spherical tip.
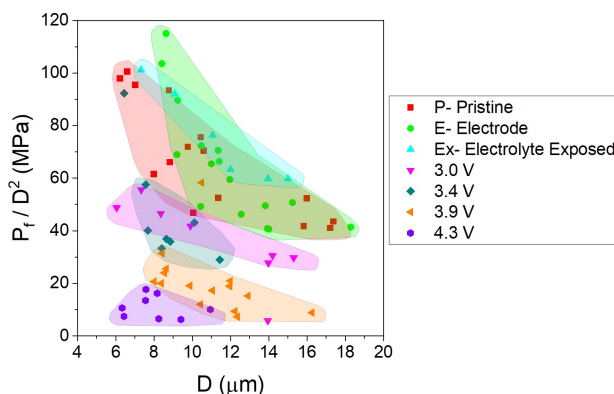

Figure 6. Indentation strength $\sigma_f = P_f/D^2$ variation with secondary particle diameter for the NMC811 secondary particles tested in Figure 5. The coloured regions represent the range of strengths measured for each type of secondary particle listed in the key. Mechanical testing was performed with the cono-spherical tip.

sample (except for cycled, and electrolyte-soaked samples where six secondary particles were measured).

The average indentation strengths, measured using the cono-spherical tip, of pristine and electrode extracted NMC811 secondary particles are similar (67±21 MPa, and 64±22 MPa respectively). The strength ranges measured for the electrode extracted secondary particles (Figure 5) are within the range measured for the pristine secondary particles indicating that the electrode fabrication process (without calendaring) and particle extraction process did not cause a significant decrease in the secondary particle strength.

The increase in average NMC811 secondary particle strength due to electrolyte soaking for 12 h (Ex) compared with the pristine (P) and electrode extracted (E) particles may be due to statistical skew (Figure 5). Figure 6 plots the measured NMC811 particle strengths as a function of secondary particle diameter. The strengths of the electrolyte exposed secondary particles are close to the strength range of the pristine and electrode extracted secondary particles. The range of electrolyte soaked secondary particle diameters tested was from 7–14 μm, whereas the range of pristine and electrode extracted secondary particle diameters was wider at 6–18 μm. Larger secondary particles have a lower indentation strength (see Figure 6) so the lack of larger particles tested would increase the average strength (see Figure 5). The minor variation in secondary particle strength may arise from defects in their internal microstructure (e. g., processing voids and cracks), or from surface film formation upon electrolyte exposure.

Cycling led to a major decrease in the average NMC811 secondary particle strength (Figure 5), with the mean particle strength measured in the discharge state after 3 cycles being (36±15 MPa), compared to the particles extracted from the uncycled electrode (64±22 MPa). The major decrease in particle strength occurred despite mild cycling conditions (0.05 C and 0.1 C, to 4.3 V vs. Li/Li$^+$). The lower strength of the discharged (3.0 V) secondary particles (36±15 MPa) compared to the uncycled electrode extracted secondary particles (64±22 MPa, Figure 5) is likely due to flaws introduced by previous formation cycles and full C/10 cycle. Flaws induced by the previous cycles could include previous intergranular fracture occurring in early stage cycling,[17] and other grain boundary defects such as rock salt formation,[5] which would result in an overall strength reduction. The results imply that mechanical weakening induced by early stage cycling will leave secondary particles vulnerable to fracture.

Upon charging (de-lithiating) NMC811 electrodes to higher potentials (3.4 V, 3.9 V, and 4.3 V vs. Li/Li$^+$) the mean strength decreased from 67±21 MPa in the pristine state to 11±4 MPa at 4.3 V. The decrease in individual secondary NMC811 secondary particle strength at higher states of charge is consistent with observations in the literature of increased intergranular fracture of secondary particles at higher states of charge.[15,16,30]

The largest strength decrease occurred between 3.4 V and 3.9 V vs. Li/Li$^+$ (from 46±15 MPa to 21±12 MPa), before the second differential capacity peak shown in Figure S7, associated with the c-axis parameter decrease. The c-axis parameter

reduction is often associated with more severe intergranular particle fracture,[31] however straining in NMC materials occurs upon the onset of delithiation, initially resulting in anisotropic strain, followed by volume change.[20,31] Measurements reported in a previous study on single crystal NMC811 suggest the decrease in secondary particle strength upon de-lithiation is accompanied by a decrease in the shear strength of the primary particles.[32] Further investigation is required to understand the cause of grain boundary weakening upon delithiation, and whether it is purely related to anisotropic strain caused by unit cell shape change,[15,20,31] or if other factors such as surface reduction are involved.

Figure 6 shows how the measured NMC secondary particle strength varies with individual secondary particle size (diameter) and state of charge. Figure 6 clearly demonstrates that secondary particle strength is reduced by cycling and thereafter by increasing degree of delithiation, with a substantial drop in secondary particle strength for NMC811 upon charging above 3.4 V. Figure 6 also demonstrates that the trend of lower strength with increasing secondary particle size is present for all measured states of charge and charge-discharge history. After charging to 4.3 V vs. Li/ Li$^+$, the largest particle measured had a diameter of 12 μm because in the weakened charged state, larger secondary particles were not mechanically stable enough to survive extraction.

The observation that larger secondary particles are mechanically weaker correlates with microstructural observations using X-ray computed tomography (XCT) by Wade et al.,[33] and micro-X-ray computed tomography (XCT) performed here (see Supporting Information) which suggest that larger secondary NMC811 secondary particles were more likely to contain internal cracks. Micro-XCT imaging performed in this study (with >1 μm resolution) found cracks in secondary particles with diameters >15 μm in uncycled electrodes. For electrodes

charged to 4.3 V vs. Li/ Li$^+$ internal cracks were found in smaller secondary particles with diameters greater than 10 μm. For secondary particles smaller than 10 μm in diameter the Micro-XCT was unable to identify cracks of <1 μm width after cycling, however then can be identified by SEM (Figure 7e and g).

The dependence of indentation strength upon secondary particle size, as measured by cono-spherical tip micro-indentation, differs to that of flat platen compression experiments (see Supporting Information) in which strength shows less sensitivity to secondary particle size (Figure 3e). As stated above flat platen compression may provide a measure of the cohesive strength in tension, whereas the maximum load measured by the cono-spherical tip indentation tests depends also upon the Mode I fracture toughness: for this reason, a size dependence is observed. As a size dependence is observed in all of the cono-spherical tip tests, insight into the how particle toughness variations during de-lithiation alters the strength of secondary particles may be provided for the states of charge studied here.

To evaluate the origin of the mechanical weakening of charged NMC811 secondary particles, in-situ SEM videos of charged NMC811 secondary particles deforming under compression were examined in detail. Figure 7 shows representative example SEM images of an uncycled NMC811 secondary particle, and NMC811 secondary particles charged to 3.0 V, 3.9 V, and 4.3 V vs. Li/ Li$^+$ on the second C/10 cycle before and after indentation. In all cases the secondary particle deformation mode remained Mode I intergranular fracture as also observed for the pristine state (e. g., Figure 7b, d, f, and h), initiating from the tip contact zone. In some cases, the growth of radial cracks was sufficient to propagate right through secondary particles and break them into fragments.

Surface cracks were present on NMC811 secondary particles after charging to 3.9 V and 4.3 V vs. Li/ Li$^+$ (Figure 7e and g)

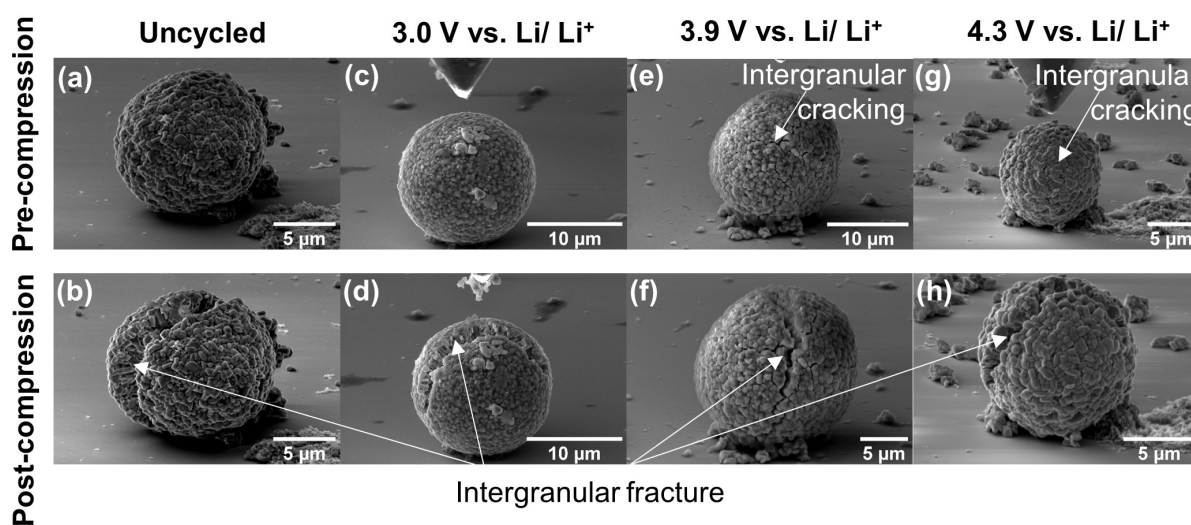## NMC811 Particles Pre- and Post- Indentation

Figure 7. Representative SEM images of NMC811 secondary particles extracted from a and b) uncycled electrodes, and electrodes charged on the second C/10 cycle to c and d) 3.0 V, e and f) 3.9 V, and g, and h) 4.3 V. a, c, e and g) were taken before microindentation with the cono-spherical tip, and b, d, f and h) after microindentation.

before indentation testing. The surface cracks in Figure 7(e and g) are between the grains (intergranular), similar to fracture initiated by the cono-spherical indenter tip, but the crack widths are much smaller. The SEM imaging only provides surface imaging so it is difficult to comment on the pre-existing fracture propagation within the particle itself, however, given the particles are still intact in Figure 7(e and g), it is unlikely the pre-existing intergranular fracture extended through the whole particle (as the tip induced fracture does).

Pre-existing surface cracks were not observed on uncycled secondary particles, and secondary particles charged to 3.0 V vs. Li/ Li$^+$ Figure 7(a and c). SEM imaging of electrode cross-sections (Supporting Information Figure S6) identified internal intergranular cracking (along mostly radial grain boundaries) in the cross-section of NMC811 secondary particles charged to 4.3 V vs. Li/ Li$^+$, but only minimal intergranular cracking in cross-sections of NMC811 secondary particles in an uncycled electrode.

Despite the presence of pre-existing cracks from cycling, compression-induced intergranular cracking in NMC811 secondary particles charged to 3.9 and 4.3 V vs. Li/ Li$^+$ originated from the contact zone, following a radial path along the direction of load away from the contact zone. In some regions, crack propagation deviated to include the pre-existing cracks (Figure 7e and g). Pre-existing internal cracks offer reduced energy paths for propagating cracks. The presence of intergranular internal cracking in charged NMC811 secondary particles correlates with the reduced strength of secondary particles charged to higher potentials (see Figure 5, and Figure 6). Furthermore, once grain boundary cracks occur within a secondary particle, the secondary particle becomes more susceptible to fracture, fragmentation and subsequent chemo-mechanical degradation during cycling.

Figure 7(b, d, f, and h) shows that intergranular fracture takes place upon loading regardless of the state of charge. The tensile fracture strength of sintered Li[Ni$_{0.33}$Mn$_{0.33}$Co$_{0.33}$]O$_2$ has been shown to increase with decreasing grain size,[34] as is typical for polycrystalline ceramics that contain flaws on the order of the grain size. Additionally, aligning the primary particles relative to one another may decrease the stresses that arise between neighbouring primary particles with different c-axis orientations.[35] A previous study obtained smaller, elongated and aligned primary particles within the secondary particle by substitution of W for Al in Ni-rich Li[Ni$_{0.885}$Co$_{0.1}$Al$_{0.015}$]O$_2$;[36] this approach was found to reduce the formation of intergranular fractures during cycling.

Conclusion

The in-situ SEM micro-indentation technique enables assessment of the fracture resistance of secondary particles, and imaging of the fracture mechanism during testing, enabling conclusions about how microstructure affects fracture propagation to be made. Compression of individual NMC811 secondary particles was carried out in-situ inside the SEM using both cono-spherical and flat platen diamond tips, mimicking differ-

ent contact stress states from sharp and flat asperities. The flat platen mimics load from a calendar mill, whilst the sharp asperity mimics the load from particle to particle contact. Finite element modelling of flat platen compression and cono-spherical indentation predicted a more uniform tensile stress distribution of lower maximum value during compression with a flat platen than for cono-spherical indentation at the same load. The lower failure loads and the decrease in average tensile stress across the particle at failure with increasing pristine secondary particle diameter in cono-spherical indentation are consistent with finite element simulations that calculate a marked tensile stress concentration below the sharp cono-spherical contact zone (Figure 3). Experimentally, the increased surface tensile stress induced by cono-spherical tip resulted in Mode I fracture, with cracks initiating near the tip and propagating intergranularly through the particle (Figure 1). Mode I fracture has been demonstrated to occur during cycling, and the presence of tensile stresses at the particle surface is consistent with intergranular fracture,[23,27] making use of the cono-spherical tip appropriate for mechanical testing studies of secondary particle assemblies.

Consistent with Mode I fracture, the secondary particle strength measured by cono-spherical indentation is dependent upon the secondary particle size in experiments using a cono-spherical tip, with smaller particles having greater particle strength than larger particles. The strength of individual NMC811 secondary particles decreases drastically after only 3 cycles (from 64±22 MPa to 36±15 MPa), implying that flaws generated during early stage cycling, even under mild cycling conditions (0.05 C/0.1 C to 4.3 V vs. Li/ Li$^+$), are enough to affect the mechanical strength of secondary particles. The strength of individual NMC811 secondary particles also decreases with increasing state of charge, with the largest decrease occurring in early stage cycling between 3.4 V and 3.9 V vs. Li/ Li$^+$ (from 46±19 MPa to 20±11 MPa- see Figure 5), prior to the c-axis contraction associated with fracture in the literature.[15,30]

The in-situ SEM microindentation technique could be quickly applied to other battery particle morphologies to assess their resistance to fracture in the future and inform synthetic approaches to more resilient cathode particles.

Experimental Section

Electrode preparation and electrochemical testing

LiNi$_{0.8}$Mn$_{0.1}$Co$_{0.1}$O$_2$ NMC811 (Targray) powders were used to manufacture electrodes through a tape casting method onto carbon coated aluminium foil (MTI). Polyvinylidene fluoride (PVDF) binder (MTI), and carbon black C65 (Timcal) conductive additive were combined in a ratio of 90 wt.% NMC811, 5 wt.% C65, and 5 wt.% PVDF.

NMC811, C65, and PVDF were weighed out in an Ar filled glove box to prevent oxidation of the NMC811, and the slurry mixed using an orbital mixer (Thinky) with N-methyl 2-pyrrolidone (NMP) (Sigma Aldrich). No ball milling was performed to minimise mechanical damage. The C65 particles and NMC811 secondary particles were added step-wise, mixing between each step, to a

10 wt.% solution of PVDF and NMP to ensure sufficient coverage of the NMC secondary particles with C65 and binder.

The slurry was spread to with a doctor blade thickness of 200 μm thickness, and dried for 1 h at 100 °C. The electrode sheet was placed into a vacuum furnace at 80 °C overnight to ensure the solvent was completely dry, and transferred into an Ar filled glove box. 12 mm electrode discs were punched out of the dried electrode tape. Calendaring was not performed to avoid calendaring induced mechanical damage.

Electrodes were assembled into half-cells using 2016 stainless steel coin cells (Cambridge Energy Solutions), using a Whatman GF/F glass fibre separator, soaked in 100 μL of $LiPF_6$ in a 50/50 volume ratio of ethylene carbonate (EC) and dimethyl carbonate (DMC) (Sigma Aldrich), a Li disc anode (8 mm diameter) (Sigma Aldrich), and a 0.5 mm thick stainless steel spacer.

The coin cells were cycled using a Maccor galvanostat. Prior to cycling, the cells were rested for 12 h. Two formation cycles were performed at C/20 between 3.0 V vs. Li/ Li$^+$, and 4.3 V vs. Li/ Li$^+$, resting for 1 h between each cycle. The cells were held at 4.3 V vs. Li/ Li$^+$ until the current dropped below C/40. After the formation cycles, the cells were cycled at C/10 between 3.0 V vs. Li/ Li$^+$ and 4.3 V vs. Li/ Li$^+$ for one complete cycle. The cells were stopped on the second charge cycle at C/10 at 3.0 V, 3.4 V, 3.9 V, and 4.3 V vs. Li/ Li$^+$ for mechanical testing. For each charge the potential was held at the respective voltage until the current dropped below C/20 to try to minimise any shock caused by stopping the applied current during charge.

Secondary particle preparation for fracture testing

All mechanical testing was performed on secondary particles mounted on a Si wafer (0.38 mm thick). The Si wafers were superglued to SEM stubs in order to avoid compliance issues caused by standard carbon tabs. Pristine NMC811 secondary particles were prepared for mechanical testing by suspending the secondary particles in ethanol using a vortex generator and drop casting onto the Si wafer.

Cycled electrodes were de-crimped and washed with 0.2 mL dimethyl carbonate (DMC) in an Ar filled glove box to remove electrolyte residues. The DMC was allowed to dry in the glove box prior to secondary particle extraction and post-mortem characterisation.

Secondary particles mounted in electrodes were extracted by dissolving the binder in NMP. Prior to soaking the electrodes were 'jet washed' with NMP from a syringe to separate electrode fragments from the current collector. The electrodes were allowed to soak for 3 days in NMP in an Ar filled glove box at room temperature. After soaking, the NMP/electrode suspension was stirred using a stir bar and heated at 80 °C for 1 h. The NMP/ NMC811 secondary particle suspensions were drop cast onto NMC wafers.

The NMC811 secondary particles studied had a secondary particle diameter range of 6–18 μm. The primary particles had an irregularly faceted morphology, and had a size distribution of 0.5–1.5 μm. An image of the fracture surface of a pristine NMC811 particle demonstrating the morphology of the primary particles is shown in Figure S6(e) in the Supporting Information.

in situ SEM mechanical testing and analysis

Mechanical testing was performed with an Alemnis microindenter mounted in an FEI Nova 450 scanning electron microscope (SEM).

All secondary electron imaging was performed with a 5 kV electron beam. The Alemnis rig was set-up with a 20° stage tilt, therefore due to the mounting position of the SEM stub in the Alemnis rig, imaging was performed at a 70° tilt to the indenter axis.

The Alemnis stage consisted of a diamond tip mounted on a piezo stack actuator allowing controlled normal force applications onto the sample. The SEM stub with the NMC811 secondary particles mounted onto the Si wafer was attached to a translation stage on the Alemnis stage, allowing the tip to be positioned directly above secondary particles for indentation. A schematic of the set-up is detailed in the Supporting Information.

Secondary particle indentation was performed with two distinct indentation tips: a Synton MDP cono-spherical pure diamond indentation tip (poisson's ratio −0.07, Young's modulus- 1140 GPa), and with a diamond flat platen (Synton MDP). NMC811 secondary particles were indented individually, ensuring that no neighbouring secondary particles in direct contact, and that no residual binder from the extraction process was imaged on the secondary particle as both phenomena could impact the measured fracture pressure. The secondary particles were indented under a ramped load control at 0.1 mN s^{-1}, measuring displacement during loading. Once the secondary particle had fractured, the tip retracted.

Data was processed using Alemnis AMMDA software. Each load curve had the load drift corrected, and the displacement corrected to zero at zero load. Load drift corrections (polynomial fitting) were applied to all data using the in-built features on the Alemnis AMMDA software. The indentation hardness at the point of fracture was calculated as the load at fracture normalised by the tip contact area. The tip contact area formula, and calibration are detailed in the Supporting Information.

To gain insight into the stress state and fracture progression within cathode secondary particles during indentation testing, finite element calculations were performed using the commercial finite element software ABAQUS, supplied by Dassault Systèmes, Cambridge.

Conflict of Interest

The authors declare no conflict of interest.

Data Availability Statement

The data that support the findings of this study are available from the corresponding author upon reasonable request.

Batteries & Supercaps

Research Article
doi.org/10.1002/batt.202300032

Chemistry Europe
European Chemical
Societies Publishing

[1] K. Mizushima, P. C. Jones, P. J. Wiseman, J. B. Solid State Ionics **1981**, 3–4 (C), 171–174.

[2] E. J. Cairns, P. Albertus, Annu. Rev. Chem. Biomol. Eng. **2010**, 1, 299–320.

[3] T. Li, X.-Z. Yuan, L. Zhang, D. Song, K. Shi, C. Bock, Electrochem. Energy Rev. **2020**, 3, 43–80.

[4] A. Mukhopadhyay, B. W. Sheldon, Prog. Mater. Sci. **2014**, 63, 58–116.

[5] C. Xu, K. Märker, J. Lee, A. Mahadevegowda, P. J. Reeves, S. J. Day, M. F. Groh, S. P. Emge, C. Ducati, B. Layla Mehdi, C. C. Tang, C. P. Grey, Nat. Mater. **2020**, 20, 84–92.

[6] R. Jung, M. Metzger, F. Maglia, C. Stinner, H. A. Gasteiger, J. Electrochem. Soc. **2017**, 164, A1361–A1377.

[7] P. Yan, J. Zheng, J. Liu, B. Wang, X. Cheng, Y. Zhang, X. Sun, C. Wang, J. G. Zhang, Nat. Energy **2018**, 3, 600–605.

[8] R. Ruess, S. Schweidler, H. Hemmelmann, G. Conforto, A. Bielefeld, D. A. Weber, J. Sann, M. T. Elm, J. Janek, J. Electrochem. Soc. **2020**, 167, 100532.

[9] P. Li, Y. Zhao, Y. Shen, S. H. Bo, J. Phys. Energy **2020**, 2, 022002.

[10] G. Conforto, R. Ruess, D. Schröder, E. Trevisanello, R. Fantin, F. H. Richter, J. Janek, J. Electrochem. Soc. **2021**, 168, 070546.

[11] H. H. Ryu, K. J. Park, C. S. Yoon, Y. K. Sun, Chem. Mater. **2018**, 30, 1155–1163.

[12] Z. Xu, M. M. Rahman, L. Mu, Y. Liu, F. Lin, J. Mater. Chem. A **2018**, 6, 21859–21884.

[13] W. M. Dose, J. K. Morzy, A. Mahadevegowda, C. Ducati, C. P. Grey, M. F. L. De Volder, J. Mater. Chem. A **2021**, 9, 23582–23596.

[14] R. Xu, L. S. de Vasconcelos, J. Shi, J. Li, K. Zhao, Exp. Mech. **2018**, 58, 549–559.

[15] L. De Biasi, A. O. Kondrakov, H. Geßwein, T. Brezesinski, P. Hartmann, J. Janek, J. Phys. Chem. C **2017**, 121, 26163–26171.

[16] E. Trevisanello, R. Ruess, G. Conforto, F. H. Richter, J. Janek, Adv. Energy Mater. **2021**, 11, 2003400.

[17] T. M. M. Heenan, A. Wade, C. Tan, J. E. Parker, D. Matras, A. S. Leach, J. B. Robinson, A. Llewellyn, A. Dimitrijevic, R. Jervis, P. D. Quinn, D. J. L. Brett, P. R. Shearing, Adv. Energy Mater. **2020**, 10, 2002655.

[18] L. S. De Vasconcelos, R. Xu, Z. Xu, J. Zhang, N. Sharma, S. R. Shah, J. Han, X. He, X. Wu, H. Sun, S. Hu, M. Perrin, X. Wang, Y. Liu, F. Lin, Y. Cui, K. Zhao, Chem. Rev. **2022**, 122, 13043–13107.

[19] Y. Mao, X. Wang, S. Xia, K. Zhang, C. Wei, S. Bak, Z. Shadike, X. Liu, Y. Yang, R. Xu, P. Pianetta, S. Ermon, E. Stavitski, K. Zhao, Z. Xu, F. Lin, X. Yang, E. Hu, Y. Liu, Adv. Funct. Mater. **2019**, 29, 1900247.

[20] J. C. Stallard, L. Wheatcroft, S. G. Booth, R. Boston, S. A. Corr, M. F. L. De Volder, B. J. Inkson, N. A. Fleck, Joule **2022**, 6, 984–1007.

[21] D. Dang, Y. Wang, Y.-T. Cheng, J. Electrochem. Soc. **2019**, 166, A2749–A2751.

[22] N. Sharma, D. Meng, X. Wu, L. S. de Vasconcelos, L. Li, K. Zhao, Extrem. Mech. Lett. **2022**, 101920.

[23] H. Tian, L. T. Gao, Z.-S. Guo, J. Electrochem. Soc. **2022**, 169, 090513.

[24] M. A. Hopcroft, W. D. Nix, T. W. Kenny, J. Microelectromechanical Syst. **2010**, 19, 229–238.

[25] W. C. Oliver, G. M. Pharr, J. Mater. Res. **1992**, 7, 1564–1580.

[26] Y. Hiramatsu, Y. Oka, Int. J. Rock Mech. Min. Sci. Geomech. Abstr. **1966**, 3, 89–90.

[27] L. Romano Brandt, J. J. Marie, T. Moxham, D. P. Förstermann, E. Salvati, C. Besnard, C. Papadaki, Z. Wang, P. G. Bruce, A. M. Korsunsky, Energy Environ. Sci. **2020**, 13, 3556–3566.

[28] K. Märker, P. J. Reeves, C. Xu, K. J. Griffith, C. P. Grey, Chem. Mater. **2019**, 31, 2545–2554.

[29] H. Liu, A. J. Naylor, A. Sreekumar Menon, W. R. Brant, K. Edström, R. Younesi, Adv. Mater. Interfaces **2020**, 7, 2000277.

[30] A. O. Kondrakov, A. Schmidt, J. Xu, H. Geßwein, R. Mönig, P. Hartmann, H. Sommer, T. Brezesinski, J. Janek, J. Phys. Chem. C **2017**, 121, 3286–3294.

[31] X. Zhao, G. Ceder, Joule **2022**, 6, 2683–2685.

[32] J. C. Stallard, S. Vema, D. S. Hall, A. R. Dennis, M. E. Penrod, C. P. Grey, V. S. Deshpande, N. A. Fleck, J. Electrochem. Soc. **2022**, 169, 040511.

[33] A. Wade, T. M. M. Heenan, M. Kok, T. Tranter, A. Leach, C. Tan, R. Jervis, D. J. L. Brett, P. R. Shearing, npj Mater. Degrad. 2022 61 **2022**, 6, 1–13.

[34] W. Huddleston, F. Dynys, A. Sehirlioglu, J. Am. Ceram. Soc. **2020**, 103, 1527–1535.

[35] X. Xu, H. Huo, J. Jian, L. Wang, H. Zhu, S. Xu, X. He, G. Yin, C. Du, X. Sun, Adv. Energy Mater. **2019**, 9, 1803963.

[36] H. Ryu, K. Park, D. R. Yoon, A. Aishova, C. S. Yoon, Y. Sun, Adv. Energy Mater. **2019**, 9, 1902698.